

Observation of Directed Flow of Hypernuclei ${}^3_{\Lambda}\text{H}$ and ${}^4_{\Lambda}\text{H}$ in $\sqrt{s_{\text{NN}}} = 3$ GeV Au+Au Collisions at RHIC

B. E. Aboona, D. M. Anderson, Y. Liu, J. Pan, and R. E. Tribble
Texas A&M University, College Station, Texas 77843

J. Adam, J. Ceska, A. Das, and O. Lomicky
Czech Technical University in Prague, FNSPE, Prague 115 19, Czech Republic

J. R. Adams, J. D. Brandenburg, T. J. Humanic, and X. Liu
Ohio State University, Columbus, Ohio 43210

G. Agakishiev, A. Aitbaev, A. Aparin, G. S. Averichev, T. G. Dedovich,
A. Kechechyan, A. A. Korobitsin, R. Lednicky, V. B. Luong, A. Mudrokh,
Y. Panebratsev, O. V. Rogachevsky, E. Shahaliev, M. V. Tokarev, and S. Vokal
Joint Institute for Nuclear Research, Dubna 141 980

I. Aggarwal, M. M. Aggarwal, A. Dhamija, L. Kumar, A. S. Nain, N. K. Pruthi, and J. Singh
Panjab University, Chandigarh 160014, India

Z. Ahammed
Variable Energy Cyclotron Centre, Kolkata 700064, India

I. Alekseev
*Alikhanov Institute for Theoretical and Experimental Physics NRC "Kurchatov Institute", Moscow 117218 and
National Research Nuclear University MEPhI, Moscow 115409*

J. Atchison, M. Daugherty, J. L. Drachenberg, and D. Isenhower
Abilene Christian University, Abilene, Texas 79699

V. Bairathi and S. Kabana
Instituto de Alta Investigación, Universidad de Tarapacá, Arica 1000000, Chile

W. Baker, K. Barish, D. Chen, M. L. Kabir, D. Kapukchyan, X. Liang, E. Loyd, A. Paul, C. Racz, R. Seto, and Y. Wu
University of California, Riverside, California 92521

J. G. Ball Cap
University of Houston, Houston, Texas 77204

P. Bhagat, A. Bhasin, A. Gupta, A. Jalotra, and M. Sharma
University of Jammu, Jammu 180001, India

S. Bhatta, S. L. Huang, R. Lacey, N. Magdy, C. Sun, Z. Yan, and C. Zhang
State University of New York, Stony Brook, New York 11794

I. G. Bordyuzhin, E. Samigullin, and D. N. Svirida
Alikhanov Institute for Theoretical and Experimental Physics NRC "Kurchatov Institute", Moscow 117218

A. V. Brandin, L. Kochenda, P. Kravtsov, G. Nigmatkulov,
V. A. Okorokov, P. Parfenov, M. Strikhanov, and A. Taranenko
National Research Nuclear University MEPhI, Moscow 115409

X. Z. Cai and B. Xi
Shanghai Institute of Applied Physics, Chinese Academy of Sciences, Shanghai 201800

H. Caines, F. A. Flor, J. W. Harris, R. Kunnawalkam Elayavalli,
T. Liu, I. Mooney, D. B. Nemes, Y. Song, and A. Tamis

Yale University, New Haven, Connecticut 06520

M. Calderón de la Barca Sánchez, D. Cebra, M. D. Harasty, B. Kimelman, and Z. W. Sweger
University of California, Davis, California 95616

I. Chakaberia, X. Dong, Y. Hu, Y. Ji, H. S. Ko, H. S. Matis,
G. Odyniec, S. Oh, H. G. Ritter, J. H. Thomas, H. Wieman, and N. Xu
Lawrence Berkeley National Laboratory, Berkeley, California 94720

B. K. Chan, Y. Cheng, H. Z. Huang, D. Neff, S. Trentalange, G. Wang, X. Wu, and Z. Xu
University of California, Los Angeles, California 90095

Z. Chang, W. W. Jacobs, H. Liu, and S. W. Wissink
Indiana University, Bloomington, Indiana 47408

J. Chen, Z. Chen, X. Gou, Y. He, C. Li, T. Lin, M. Nie, N. R. Sahoo, Y. Shi, X. Wang,
Z. Wang, Q. H. Xu, Y. Xu, G. Yan, C. Yang, Q. Yang, L. Yi, Y. Yu, and J. Zhang
Shandong University, Qingdao, Shandong 266237

J. H. Chen, S. Choudhury, W. He, L. Ma, Y. G. Ma, T. Shao, D. Y. Shen, Q. Y. Shou, J. Zhao, and C. Zhou
Fudan University, Shanghai, 200433

J. Cheng, X. Huang, Y. Huang, K. Kang, Y. Li, Z. Qin, Y. Wang, Z. G. Xiao, and X. Zhu
Tsinghua University, Beijing 100084

W. Christie, X. Chu, L. Didenko, J. C. Dunlop, O. Eyser, Y. Fisyak, K. Kauder, H. W. Ke, A. Kiselev,
J. M. Landgraf, A. Lebedev, J. H. Lee, N. Lewis, T. Ljubicic, R. S. Longacre, R. Ma, A. S. Nunes,
A. Ogawa, B. S. Page, R. Pak, L. Ruan, W. B. Schmidke, P. V. Shanmuganathan, A. H. Tang, P. Tribedy,
Z. Tu, T. Ullrich, G. Van Buren, F. Videbæk, J. C. Webb, Z. Xu, K. Yip, Z. Zhang, and M. Zhao
Brookhaven National Laboratory, Upton, New York 11973

H. J. Crawford, J. Engelage, E. G. Judd, J. M. Nelson, and C. Perkins
University of California, Berkeley, California 94720

G. Dale-Gau, O. Evdokimov, T. Huang, G. Wilks, Z. Ye, and Z. Zhang
University of Illinois at Chicago, Chicago, Illinois 60607

I. M. Deppner, Y. H. Leung, Y. Söhngen, and P. C. Weidenkaff
University of Heidelberg, Heidelberg 69120, Germany

A. A. Derevschikov, N. G. Minaev, D. A. Morozov, and L. V. Nogach
NRC "Kurchatov Institute", Institute of High Energy Physics, Protvino 142281

L. Di Carlo, M. Kelsey, W. J. Llope, G. McNamara, J. Putschke,
N. Raha, D. J. Stewart, V. Verkest, and S. A. Voloshin
Wayne State University, Detroit, Michigan 48201

P. Dixit, Md. Nasim, A. K. Sahoo, and N. Sharma
Indian Institute of Science Education and Research (IISER), Berhampur 760010, India

E. Duckworth, D. Keane, Y. Liang, S. Margetis, S. K. Radhakrishnan, and A. I. Sheikh
Kent State University, Kent, Ohio 44242

G. Eppley, F. Geurts, Y. Han, C. Jin, W. Li, I. Upsal, and Z. Ye
Rice University, Houston, Texas 77251

- S. Esumi, M. Isshiki, T. Niida, R. Nishitani, T. Nonaka, K. Okubo, H. Sako, S. Sato, and T. Todoroki
University of Tsukuba, Tsukuba, Ibaraki 305-8571, Japan
- A. Ewigleben, A. G. Knospe, T. Protzman, and C. A. Tomkiel
Lehigh University, Bethlehem, Pennsylvania 18015
- R. Fatemi, H. Harrison, and M. A. Rosales Aguilar
University of Kentucky, Lexington, Kentucky 40506-0055
- S. Fazio
University of Calabria & INFN-Cosenza, Italy
- C. J. Feng, H. Huang, Y. Yang, and Z. J. Zhang
National Cheng Kung University, Tainan 70101
- Y. Feng, C. W. Robertson, B. Srivastava, B. Stringfellow, F. Wang, and W. Xie
Purdue University, West Lafayette, Indiana 47907
- E. Finch
Southern Connecticut State University, New Haven, Connecticut 06515
- C. Fu, Y. Huang, F. Liu, H. Liu, L. Liu, Z. Liu, X. F. Luo, K. Mi, S. S. Shi,
Y. Wang, J. Wu, Y. Xu, D. Zhang, Y. Zhang, S. Zhou, and Y. Zhou
Central China Normal University, Wuhan, Hubei 430079
- N. Ghimire, N. S. Lukow, J. D. Nam, B. R. Pokhrel, M. Posik, A. Quintero, and B. Sorrow
Temple University, Philadelphia, Pennsylvania 19122
- A. Gibson, D. Grosnick, and T. D. S. Stanislaus
Valparaiso University, Valparaiso, Indiana 46383
- K. Gopal, C. Jena, R. Sharma, S. R. Sharma, and P. Sinha
Indian Institute of Science Education and Research (IISER) Tirupati, Tirupati 517507, India
- A. Hamed
American University of Cairo, New Cairo 11835, New Cairo, Egypt
- X. H. He, C. Hu, Q. Hu, S. Kumar, C. Liu, T. Lu, A. K. Pandey,
H. Qiu, S. Singha, X. Sun, J. Wu, X. Zhang, Y. Zhang, and F. Zhao
Institute of Modern Physics, Chinese Academy of Sciences, Lanzhou, Gansu 730000
- J. Jia
*Brookhaven National Laboratory, Upton, New York 11973 and
State University of New York, Stony Brook, New York 11794*
- X. Ju, C. Li, X. Li, Y. Li, Z. Li, M. Shao, K. Shen, F. Si, Y. Su,
Y. Sun, Z. Tang, Y. Wang, W. Zha, S. Zhang, Y. Zhang, and J. Zhou
University of Science and Technology of China, Hefei, Anhui 230026
- D. Kalinkin
*University of Kentucky, Lexington, Kentucky 40506-0055 and
Brookhaven National Laboratory, Upton, New York 11973*
- D. Mallick, B. Mohanty, and A. Pandav
National Institute of Science Education and Research, HBNI, Jatni 752050, India
- J. A. Mazer, T. Pani, D. Roy, and S. Salur

Rutgers University, Piscataway, New Jersey 08854

M. I. Nagy
ELTE Eötvös Loránd University, Budapest, Hungary H-1117

R. L. Ray
University of Texas, Austin, Texas 78712

N. Schmitz and P. Seyboth
Max-Planck-Institut für Physik, Munich 80805, Germany

J. Seger and D. Tlustý
Creighton University, Omaha, Nebraska 68178

N. Shah
Indian Institute Technology, Patna, Bihar 801106, India

M. J. Skoby
*Ball State University, Muncie, Indiana, 47306 and
Purdue University, West Lafayette, Indiana 47907*

Y. Sun, J. S. Wang, and H. Xu
Huzhou University, Huzhou, Zhejiang 313000

T. Tarnowsky and G. D. Westfall
Michigan State University, East Lansing, Michigan 48824

O. D. Tsai
*University of California, Los Angeles, California 90095 and
Brookhaven National Laboratory, Upton, New York 11973*

C. Y. Tsang
*Kent State University, Kent, Ohio 44242 and
Brookhaven National Laboratory, Upton, New York 11973*

D. G. Underwood
*Argonne National Laboratory, Argonne, Illinois 60439 and
Valparaiso University, Valparaiso, Indiana 46383*

A. N. Vasiliev
*NRC "Kurchatov Institute", Institute of High Energy Physics, Protvino 142281 and
National Research Nuclear University MEPhI, Moscow 115409*

S. Yang
South China Normal University, Guangzhou, Guangdong 510631

M. Zurek
Argonne National Laboratory, Argonne, Illinois 60439

M. Zyzak
Frankfurt Institute for Advanced Studies FIAS, Frankfurt 60438, Germany
(STAR Collaboration)

We report here the first observation of directed flow (v_1) of the hypernuclei ${}^3_{\Lambda}\text{H}$ and ${}^4_{\Lambda}\text{H}$ in mid-central Au+Au collisions at $\sqrt{s_{\text{NN}}} = 3$ GeV at RHIC. These data are taken as part of the beam energy scan program carried out by the STAR experiment. From 165×10^6 events in 5%-40% centrality, about 8400 ${}^3_{\Lambda}\text{H}$ and 5200 ${}^4_{\Lambda}\text{H}$ candidates are reconstructed through two- and three-body decay channels. We observe that these hypernuclei exhibit significant directed flow. Comparing to

that of light nuclei, it is found that the midrapidity v_1 slopes of ${}^3_\Lambda\text{H}$ and ${}^4_\Lambda\text{H}$ follow baryon number scaling, implying that the coalescence is the dominant mechanism for these hypernuclei production in the 3 GeV Au+Au collisions.

When a nucleon is replaced by a hyperon (*e.g.*, Λ , Σ) with strangeness $S = -1$, a nucleus is transformed into a hypernucleus which allows for the study of the hyperon-nucleon (Y - N) interaction. It is well known that two-body Y - N and three-body Y - N - N interactions, especially at high baryon density, are essential for understanding the inner structure of compact stars [1, 2]. New results on precision measurements of Λ - p elastic scattering from Jefferson Lab [3] and Σ^- - p elastic scattering from J-PARC [4, 5] became available recently, which may help to constrain the equation of state of high density matter inside a neutron star. Until recently, almost all hypernuclei measurements have been carried out with light particle (*e.g.*, e , π^+ , K^-) induced reactions [6–8], where the Y - N interaction around the saturation density is analyzed from spectroscopic properties of hypernuclei.

Utilizing hypernuclei production in heavy-ion collisions to study the Y - N interaction and the properties of QCD matter has been a subject of interest in the past decades [9–13]. However, due to limited statistics, measurements have been mainly focused on the light hypernuclei lifetime, binding energy and production yields [12, 14, 15]. Thermal model [16] and hadronic transport model with coalescence afterburner [17, 18] calculations have predicted abundant production of light hypernuclei in high-energy nuclear collisions, especially at high baryon density. Anisotropic flow has been commonly used for studying the properties of matter created in high energy nuclear collisions. Because of its genuine sensitivity to early collision dynamics [19–22], the first order coefficient of the Fourier expansion of the azimuthal distribution in the momentum space, v_1 , also called the directed flow, has been analyzed for many particles species ranging from π mesons to light nuclei [23–28]. Collective flow is driven by pressure gradients created in such collisions. Hence, measurements of hypernuclei collectivity make it possible to study the Y - N interactions in the QCD equation of state at high baryon density.

In this Letter, we report the first observation of directed flow, v_1 , of ${}^3_\Lambda\text{H}$ and ${}^4_\Lambda\text{H}$ in center-of-mass energy $\sqrt{s_{\text{NN}}} = 3$ GeV Au+Au collisions. The data were collected by the STAR experiment at RHIC with the fixed-target (FXT) setup in 2018. A gold beam of energy 3.85 GeV/u is bombarded on a gold target of thickness 1% interaction length, located at the entrance of STAR’s time-projection chamber (TPC) [29]. The TPC, which is the main tracking detector in STAR, is 4.2 m long and 4 m in diameter, positioned inside a 0.5 T solenoidal magnetic field along the beam direction. The collision vertex position of each event along the beam direction, V_z , is required to be within ± 2 cm of the target posi-

tion. An additional requirement on the collision vertex position to be within a radius r of less than 2 cm is imposed to eliminate background events from interactions with the beam pipe. Beam-beam counters (BBC) [30] and the time-of-flight (TOF) detector [31] are used to obtain the minimum bias (MB) trigger condition. After event selection, a total of 2.6×10^8 MB events are used for further analysis.

The centrality is determined using the charged particle multiplicity distribution within the pseudorapidity region $-2 < \eta < 0$ together with Monte Carlo (MC) Glauber calculations [32, 33]. The directed flow (v_1) is measured with respect to the first-order event plane, determined by the event plane detector (EPD) [34] which covers $-5.3 < \eta < -2.6$ for the FXT setup. For this analysis, a relatively wide centrality range, 5%-40%, is selected where both the event plane resolution and the hypernuclei yield are maximized. The event plane resolution in the centrality range is 40%-75% [35]. Detailed information on the event plane resolution can be found in the Supplemental Material [36].

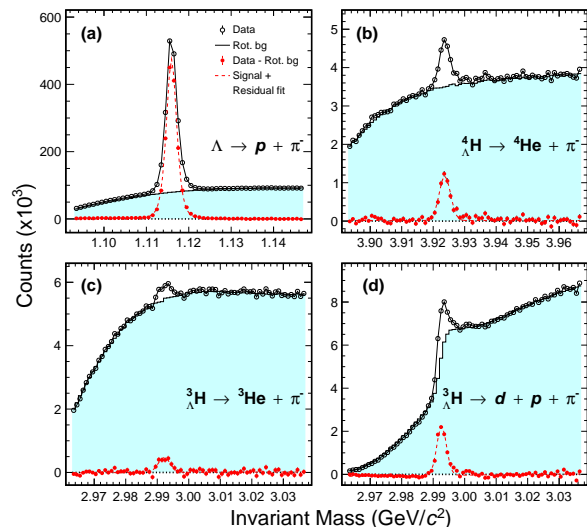


FIG. 1. Reconstructed Λ hyperon and hypernuclei invariant mass distributions from $\sqrt{s_{\text{NN}}} = 3$ GeV Au+Au collisions in the corresponding pr - y regions listed in Table I. While top panels are for $\Lambda \rightarrow p + \pi^-$ and ${}^4_\Lambda\text{H} \rightarrow {}^4\text{He} + \pi^-$, bottom panels represent the hypertriton two-body decay ${}^3_\Lambda\text{H} \rightarrow {}^3\text{He} + \pi^-$ and three-body decay ${}^3_\Lambda\text{H} \rightarrow d + p + \pi^-$, respectively. Combinatorial backgrounds, shown as histograms, are constructed by rotating decay daughter particles. Background-subtracted invariant mass distributions are shown as filled circles.

In order to ensure high track quality, we require that the number of TPC points used in the track fitting (nHitsFit) to be larger than 15 (out of a maximum of

45). ${}^3_{\Lambda}\text{H}$ is reconstructed via both two-body and three-body decays ${}^3_{\Lambda}\text{H} \rightarrow {}^3\text{He} + \pi^-$ and ${}^3_{\Lambda}\text{H} \rightarrow d + p + \pi^-$, while ${}^4_{\Lambda}\text{H}$ is reconstructed via the two-body decay channel, ${}^4_{\Lambda}\text{H} \rightarrow {}^4\text{He} + \pi^-$. Charged particles, including π^- , p , d , ${}^3\text{He}$ and ${}^4\text{He}$ are selected based on the ionization energy loss (dE/dx) measured in the TPC as a function of rigidity ($p/|q|$), where p and q are the momentum and charge of the particle. The secondary decay topology is reconstructed using the KFParticle package based on a Kalman filter method [37, 38]. The package also utilizes the covariance matrix of reconstructed tracks to construct a set of topological variables. Selection cuts on these variables are placed on hypernuclei candidates to enhance the signal significance. Figure 1 shows the reconstructed invariant mass distributions for Λ , ${}^3_{\Lambda}\text{H}$ and ${}^4_{\Lambda}\text{H}$, which are reconstructed using various decay channels in the corresponding transverse momentum p_T -rapidity y regions as listed in Table I. Combinatorial background is estimated by rotating decay particles through a random angle between 10° and 350° . For the Λ , the π^- is rotated. For the ${}^3(4)_{\Lambda}\text{H}$ two-body decay, the ${}^3(4)\text{He}$ is rotated, and for the ${}^3_{\Lambda}\text{H}$ three-body decay, the deuteron is rotated. The combinatorial background, shown as the shaded region, is normalized in the invariant mass region: (1.14, 1.16), (3.01, 3.04), and (3.95, 4.0) GeV/c^2 for Λ , ${}^3_{\Lambda}\text{H}$ and ${}^4_{\Lambda}\text{H}$, respectively. The background-subtracted invariant mass distribution (filled circles) in each panel is fitted with a linear function plus a student-t distribution for Λ and a Gaussian distribution for hypernuclei to extract the signal count. In total, 8400 ${}^3_{\Lambda}\text{H}$ and 5200 ${}^4_{\Lambda}\text{H}$ reconstructed hypernuclei from the 5%-40% centrality bin are used for further analysis.

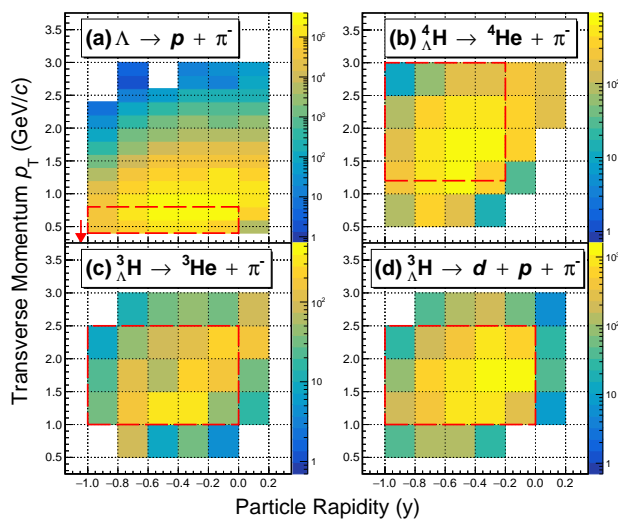


FIG. 2. Λ hyperon and hypernuclei acceptance, shown in p_T versus y , from the $\sqrt{s_{\text{NN}}} = 3$ GeV Au+Au collisions. Dashed rectangular boxes illustrate the acceptance regions used for directed flow analysis, and the red arrow in panel (a) represents the target rapidity ($y_{\text{target}} = -1.045$).

TABLE I. p_T - y acceptance windows of light nuclei, Λ hyperon and hypernuclei used for directed flow analysis.

Mass number (A)	Particle	p_T (GeV/c)	y
1	Λ, p	(0.4, 0.8)	(-1.0, 0.0)
2	d	(0.8, 1.6)	(-1.0, 0.0)
3	${}^3_{\Lambda}\text{H}$	(1.0, 2.5)	(-1.0, 0.0)
	$t, {}^3\text{He}$	(1.2, 2.4)	(-1.0, -0.1)
4	${}^4_{\Lambda}\text{H}$	(1.2, 3.0)	(-1.0, -0.2)
	${}^4\text{He}$	(1.6, 3.2)	(-1.0, -0.2)

Figure 2 shows the p_T versus y acceptance of the reconstructed Λ , ${}^3_{\Lambda}\text{H}$, and ${}^4_{\Lambda}\text{H}$ candidates in the center-of-mass frame. Following the established convention [39], the negative sign is assigned to v_1 in the rapidity region of $y < 0$. The p_T - y acceptance windows used for our analysis are tabulated in Table I and also indicated in Fig. 2.

For p_T -integrated v_1 measurements, the p_T -dependent reconstruction efficiency needs to be accounted for, which is estimated by the embedding method in STAR analyses [12, 40]. Monte Carlo generated hyperons and hypernuclei are passed through the GEANT3 simulation of the STAR detector. The simulated TPC response is then embedded into data, and the whole event is processed and analyzed using the same procedure as in the data analysis. The two-dimensional reconstruction efficiency, including the detector acceptance, in p_T - y are obtained for each decay channel, and applied to candidates in the data accordingly [41]. Kinematically, the three-body decay of ${}^3_{\Lambda}\text{H}$ is very similar to the background of correlated $d + \Lambda$ due to the very small Λ separation energy of ${}^3_{\Lambda}\text{H}$. Such correlated $d + \Lambda$ pairs that pass the ${}^3_{\Lambda}\text{H}$ three-body decay topological cuts are subtracted statistically (For details, see Fig. 3 in the Supplemental Material [36], which includes [42]). The ${}^3_{\Lambda}\text{H}$ signal fraction within the invariant mass window (2.988, 2.998) GeV/c^2 and rapidity range (-1.0, 0.0) is estimated to be 0.69 ± 0.03 .

The directed flow of Λ , ${}^3_{\Lambda}\text{H}$, and ${}^4_{\Lambda}\text{H}$ are extracted with the event plane method [43]. In each rapidity bin, the azimuthal angle with respect to the reconstructed event plane ($\Phi = \Phi' - \Psi_1$) is further divided into four equal bins with a width of $\pi/4$, where Φ' and Ψ_1 are the azimuth angle of a particle candidate and the first order event plane, respectively. After applying the reconstruction efficiency correction, the azimuthal angle distributions are fitted with a function $f(\Phi) = c_0[1 + 2v_1^{\text{obs}} \cdot \cos(\Phi) + 2v_2^{\text{obs}} \cdot \cos(2\Phi)]$, where c_0 , v_1^{obs} and v_2^{obs} are fitting parameters, and correspond to the normalization constant, the observed directed and the elliptic flow, respectively. To obtain the final v_1 in a wide centrality range of 5%-40% centrality in this analysis, the observed directed flow v_1^{obs} needs to be corrected for the average event plane resolution $\langle 1/R \rangle$ [43], i.e., $v_1 = v_1^{\text{obs}} \cdot \langle 1/R \rangle$, and $\langle 1/R \rangle = \sum_i (N_i/R_i) / \sum_i N_i$, where N_i and R_i stand for the number of particle candidates and the first order event plane resolution in the i th centrality bin, respec-

tively.

The resulting Λ hyperon and hypernuclei $v_1(y)$, from 5%-40% midcentral Au+Au collisions at $\sqrt{s_{NN}} = 3$ GeV, are shown in Fig. 3. For comparison, the $v_1(y)$ of p , d , t , ${}^3\text{He}$ and ${}^4\text{He}$ from the same data [44] are shown as open symbols. $v_1(y)$ of Λ , p , d , t , ${}^3\text{He}$ and ${}^4\text{He}$ are fitted with a third-order polynomial function $v_1(y) = ay + by^3$ in the rapidity ranges listed in Table I, where a , which stands for the midrapidity slope $dv_1/dy|_{y=0}$, and b are fitting parameters. Because of limited statistics, the hypernuclei $v_1(y)$ distributions are fitted with a linear function $v_1(y) = ay$, in the rapidity range $-1.0 < y < 0.0$. The linear terms for light nuclei are plotted as dashed lines in the positive rapidity region, while for Λ , ${}^3\Lambda\text{H}$, and ${}^4\Lambda\text{H}$, they are shown by the yellow-red lines in the corresponding panels. The Λ result is close to that of the proton, and hypernuclei $v_1(y)$ distributions are also similar to those light nuclei with the same mass numbers. This is the first observation of significant hypernuclei directed flow in high-energy nuclear collisions.

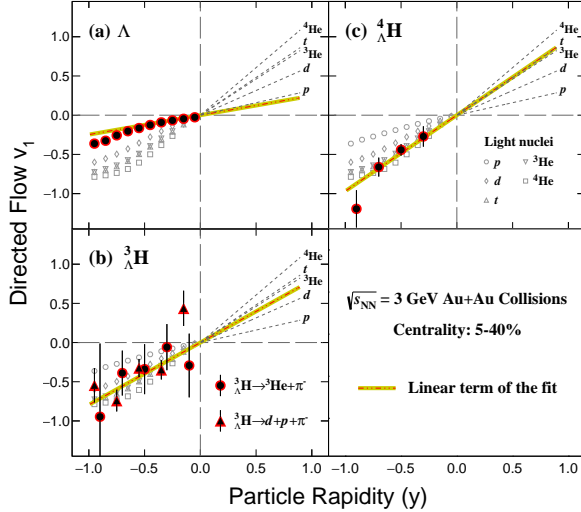


FIG. 3. Λ hyperon and hypernuclei directed flow v_1 , shown as a function of rapidity, from the $\sqrt{s_{NN}} = 3$ GeV 5%-40% midcentral Au+Au collisions. In the case of ${}^3\Lambda\text{H}$ v_1 , both two-body (dots) and three-body (triangles) decays are used. The linear terms of the fitting for Λ , ${}^3\Lambda\text{H}$ and ${}^4\Lambda\text{H}$ are shown as the yellow-red lines. The rapidity dependence of v_1 for p , d , t , ${}^3\text{He}$, and ${}^4\text{He}$ are also shown as open markers (circles, diamonds, up triangles, down triangles and squares), and the linear terms of the fitting results are shown as dashed lines in the positive rapidity region [44].

Systematic uncertainties are estimated by varying track selection criteria for particle identification, as well as cuts on the topological variables used in the KFPackage [37]. Major contributors to the systematic uncertainty are listed in Table II. As one can see, the dominant sources of systematic uncertainty are from hypernuclei candidate selection, estimated by varying topological cuts and nHitsFit. Event plane resolution de-

termination also contributes 1.4% [41]. Assuming these sources are uncorrelated, the total systematic uncertainty is obtained by adding them together quadratically. In the case of the ${}^3\Lambda\text{H}$ three-body decay, the fraction of the correlated $d\Lambda$ contamination has been analyzed in each rapidity bin. Its systematic uncertainty contribution to the final v_1 slope is negligible.

TABLE II. Sources of systematic uncertainties for midrapidity slope $dv_1/dy|_{y=0}$ of ${}^3\Lambda\text{H}$ and ${}^4\Lambda\text{H}$.

Source	${}^3\Lambda\text{H}$		${}^4\Lambda\text{H}$
	two-body	three-body	two-body
Topological cuts	1.3%	9.4%	8.0%
nHitsFit	9.0%		<1.0%
EP resolution	1.4%		1.4%
Total	13.1%		8.3%

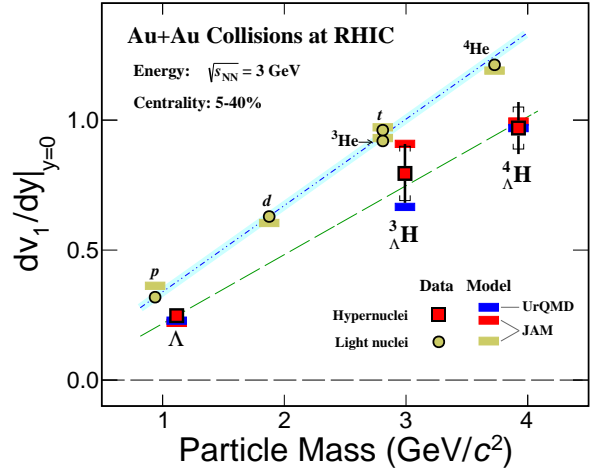


FIG. 4. Mass dependence of the midrapidity v_1 slope, $dv_1/dy|_{y=0}$, for Λ , ${}^3\Lambda\text{H}$ and ${}^4\Lambda\text{H}$ from the $\sqrt{s_{NN}} = 3$ GeV 5%-40% midcentral Au+Au collisions. The statistical and systematic uncertainties are presented by vertical lines and square brackets, respectively. The slopes of p , d , t , ${}^3\text{He}$, and ${}^4\text{He}$ from the same collisions are shown as black circles. The blue and dashed green lines are the results of a linear fit to the measured light nuclei and hypernuclei v_1 slopes, respectively. For comparison, calculations of transport models plus coalescence afterburner are shown as gold and red bars from the JAM model, and blue bars from the UrQMD model.

The results of the midrapidity slope dv_1/dy for Λ , ${}^3\Lambda\text{H}$ (both two- and three-body decays) and ${}^4\Lambda\text{H}$ are shown in Fig. 4, as filled squares, as a function of particle mass. For comparison, v_1 slopes of p , d , t , ${}^3\text{He}$ and ${}^4\text{He}$ from the same 5%-40% $\sqrt{s_{NN}} = 3$ GeV Au+Au collisions are shown as open circles. The Λ hyperon and hypernuclei slopes dv_1/dy are all systematically lower than the nuclei of same mass numbers. Linear fits ($f = a + b$ mass) are performed on the mass dependence of dv_1/dy for both light nuclei and hypernuclei. For light nuclei, only statistical uncertainties are used in the fit, while statistical and

systematic uncertainties are used for hypernuclei. The slope parameters b are 0.3323 ± 0.0003 for light nuclei and 0.27 ± 0.04 for hypernuclei. As one can see, their slopes are similar within uncertainties.

Using transport models JAM [22, 45] and UrQMD [21], $v_1(y)$ of Λ and hypernuclei are simulated for the $\sqrt{s_{NN}} = 3$ GeV Au+Au collisions within the same centrality and kinematic acceptance used in data analysis. For comparison, similar calculations are performed for light nuclei. The simulation is done in two steps: (i) using the JAM model (with momentum-dependent potential) and UrQMD model (without momentum-dependent potential) in the mean field mode with the incompressibility $\kappa = 380$ MeV to produce neutrons, protons, and Λ s at kinetic freeze-out; (ii) forming hypernuclei through the coalescence of Λ and nucleons, similar to the light nuclei production with the coalescence procedure discussed in [44]. The probability for hypernuclei production is dictated by coalescence parameters of relative momenta $\Delta p < 0.12$ (0.3) GeV/itc and relative distance $\Delta r < 4$ fm in the rest frame of $np\Lambda$ ($nnp\Lambda$) for ${}^3_\Lambda\text{H}$ (${}^4_\Lambda\text{H}$). These parameters are chosen such that the hypernuclei yields at midrapidity can be described [12]. The rapidity dependences of v_1 from the model calculations are then fitted with a third-order polynomial function within the rapidity interval $-1.0 \leq y \leq 0.0$. The resulting midrapidity slopes are shown in Fig. 4 as red and blue bars for JAM and UrQMD models, respectively. In the figure, results for light nuclei from JAM are also presented as gold bars.

Both transport models (JAM and UrQMD) plus coalescence afterburner calculations for hypernuclei are in agreement with data within uncertainties. Interactions among baryons and strange baryons are important ingredients in the transport models, especially in the high baryon density region [46, 47]. The properties of the medium are determined by such interactions. In addition, the yields of hypernuclei, if created via the coalescence process, are also strongly affected by the hyperon and nucleon interactions. In our treatment, the coalescence parameters used (Δr , Δp) reflect the production probability determined by N - N and Y - N interactions [18, 48, 49]. The mass dependence of the $v_1(y)$ slope implies that coalescence might be the dominant mechanism for hypernuclei production in such heavy-ion collisions. The mass dependence of the hypernuclei v_1 slope also seems to be similar to that of light nuclei, as shown in Fig. 4, although it may not necessarily be so due to the differences in N - N and Y - N interactions. Clearly, precise data on hypernuclei collectivity will yield invaluable insights on Y - N interactions at high baryon density.

This is the first report of the collectivity of hypernuclei in heavy-ion collisions. Hydrodynamically, collective motion is driven by pressure gradients created in such collisions. This letter opens up a new direction for studying Y - N interaction under finite pressure [50]. This is important for making the connection between nuclear collisions

and the equation of state which governs the inner structure of compact stars.

To summarize, we report the first observation of hypernuclei ${}^3_\Lambda\text{H}$ and ${}^4_\Lambda\text{H}$ v_1 from $\sqrt{s_{NN}} = 3$ GeV midcentral 5%-40% Au+Au collisions at RHIC. The rapidity dependences of their v_1 are compared with those of Λ , p , d , t , ${}^3\text{He}$ and ${}^4\text{He}$ in the same collisions. It is found that, within uncertainties, the mass dependent v_1 slope of hypernuclei, ${}^3_\Lambda\text{H}$ and ${}^4_\Lambda\text{H}$ is similar to that of light nuclei, implying that they follow the baryon mass scaling. Calculations from transport models (JAM and UrQMD) plus coalescence afterburner can qualitatively reproduce the rapidity dependence of v_1 and the mass dependence of the v_1 slope. These observations suggest that coalescence of nucleons and hyperon Λ could be the dominant mechanism for the hypernuclei ${}^3_\Lambda\text{H}$ and ${}^4_\Lambda\text{H}$ production in the 3 GeV collisions. Model calculations suggest that baryon density at freeze-out may depend on collision energy [51–53]. High statistics data at different energies, especially at the high baryon density region, will help in extracting the information on Y - N interaction and possibly its density dependence in the future.

We thank Dr. Y. Nara and Dr. J. Steinheimer for insightful discussions. We thank the RHIC Operations Group and RCF at BNL, the NERSC Center at LBNL, and the Open Science Grid consortium for providing resources and support. This work was supported in part by the Office of Nuclear Physics within the U.S. DOE Office of Science, the U.S. National Science Foundation, National Natural Science Foundation of China, Chinese Academy of Science, the Ministry of Science and Technology of China and the Chinese Ministry of Education, the Higher Education Sprout Project by Ministry of Education at NCKU, the National Research Foundation of Korea, Czech Science Foundation and Ministry of Education, Youth and Sports of the Czech Republic, Hungarian National Research, Development and Innovation Office, New National Excellency Programme of the Hungarian Ministry of Human Capacities, Department of Atomic Energy and Department of Science and Technology of the Government of India, the National Science Centre and WUT ID-UB of Poland, the Ministry of Science, Education and Sports of the Republic of Croatia, German Bundesministerium für Bildung, Wissenschaft, Forschung und Technologie (BMBF), Helmholtz Association, Ministry of Education, Culture, Sports, Science, and Technology (MEXT) and Japan Society for the Promotion of Science (JSPS).

-
- [1] D. Gerstung, N. Kaiser, and W. Weise, *Eur. Phys. J. A* **56**, 175 (2020).
 - [2] D. Lonardonì, A. Lovato, S. Gandolfi, and F. Pederiva, *Phys. Rev. Lett.* **114**, 092301 (2015).
 - [3] J. Rowley *et al.* (CLAS Collaboration), *Phys. Rev. Lett.*

- 127**, 272303 (2021).
- [4] K. Miwa *et al.* (J-PARC E40 Collaboration), Phys. Rev. C **104**, 045204 (2021).
- [5] K. Miwa *et al.* (J-PARC E40 Collaboration), Phys. Rev. Lett. **128**, 072501 (2022).
- [6] A. Gal, E. V. Hungerford, and D. J. Millener, Rev. Mod. Phys. **88**, 035004 (2016).
- [7] O. Hashimoto and H. Tamura, Prog. Part. Nucl. Phys. **57**, 564 (2006).
- [8] L. Tang *et al.* (HKS Collaboration), Phys. Rev. C **90**, 034320 (2014).
- [9] B. I. Abelev *et al.* (STAR Collaboration), Science **328**, 58 (2010).
- [10] S. Acharya *et al.* (ALICE Collaboration), Phys. Lett. B **797**, 134905 (2019).
- [11] L. Adamczyk *et al.* (STAR Collaboration), Phys. Rev. C **97**, 054909 (2018).
- [12] M. Abdallah *et al.* (STAR Collaboration), Phys. Rev. Lett. **128**, 202301 (2022).
- [13] T. R. Saito *et al.*, Nat. Rev. Phys. **3**, 803 (2021).
- [14] J. Chen, D. Keane, Y.-G. Ma, A. Tang, and Z. Xu, Phys. Rep. **760**, 1 (2018).
- [15] J. Adam *et al.* (STAR Collaboration), Nat. Phys. **16**, 409 (2020).
- [16] A. Andronic, P. Braun-Munzinger, J. Stachel, and H. Stocker, Phys. Lett. B **697**, 203 (2011).
- [17] J. Steinheimer *et al.*, Phys. Lett. B **714**, 85 (2012).
- [18] J. Aichelin *et al.*, Phys. Rev. C **101**, 044905 (2020).
- [19] C. M. Hung and E. V. Shuryak, Phys. Rev. Lett. **75**, 4003 (1995).
- [20] J. Brachmann *et al.*, Phys. Rev. C **61**, 024909 (2000).
- [21] J. Steinheimer, J. Auvinen, H. Petersen, M. Bleicher, and H. Stöcker, Phys. Rev. C **89**, 054913 (2014).
- [22] Y. Nara, H. Niemi, A. Ohnishi, and H. Stöcker, Phys. Rev. C **94**, 034906 (2016).
- [23] L. Adamczyk *et al.* (STAR Collaboration), Phys. Rev. Lett. **112**, 162301 (2014).
- [24] L. Adamczyk *et al.* (STAR Collaboration), Phys. Rev. Lett. **120**, 062301 (2018).
- [25] J. Adam *et al.* (STAR Collaboration), Phys. Rev. C **102**, 044906 (2020).
- [26] L. Adamczyk *et al.* (STAR Collaboration), Phys. Rev. C **88**, 014902 (2013).
- [27] J. Adam *et al.* (STAR Collaboration), Phys. Rev. C **103**, 034908 (2021).
- [28] A. Bzdak *et al.*, Phys. Rep. **853**, 1 (2020).
- [29] M. Anderson *et al.*, Nucl. Instrum. Methods Phys. Res., Sect. A **499**, 659 (2003).
- [30] C. A. Whitten (STAR Collaboration), AIP Conf. Proc. **980**, 390 (2008).
- [31] W. J. Llope (STAR Collaboration), Nucl. Instrum. Methods Phys. Res., Sect. A **661**, S110 (2012).
- [32] M. L. Miller, K. Reygers, S. J. Sanders, and P. Steinberg, Annu. Rev. Nucl. Part. Sci. **57**, 205 (2007).
- [33] B. I. Abelev *et al.* (STAR Collaboration), Phys. Rev. C **81**, 024911 (2010).
- [34] J. Adams *et al.*, Nucl. Instrum. Methods Phys. Res., Sect. A **968**, 163970 (2020).
- [35] M. S. Abdallah *et al.* (STAR Collaboration), Phys. Lett. B **827**, 137003 (2022).
- [36] See Supplemental Material at <http://link.aps.org/supplemental/10.1103/PhysRevLett.130.212301> for the purity of $^3\Lambda$ H three-body decay.
- [37] I. Kisel (CBM Collaboration), J. Phys. Conf. Ser. **1070**, 012015 (2018).
- [38] M. Zyzak, Online selection of short-lived particles on many-core computer architectures in the CBM experiment at FAIR, Ph.D. thesis, Frankfurt University, 2016.
- [39] H. Liu *et al.* (E895 Collaboration), Phys. Rev. Lett. **84**, 5488 (2000).
- [40] J. Adam *et al.* (STAR Collaboration), Phys. Rev. C **102**, 034909 (2020).
- [41] M. S. Abdallah *et al.* (STAR Collaboration), Phys. Lett. B **827**, 137003 (2022).
- [42] J. Haidenbauer, Phys. Rev. C **102**, 034001 (2020).
- [43] H. Masui, A. Schmah, and A. M. Poskanzer, Nucl. Instrum. Methods Phys. Res., Sect. A **833**, 181 (2016).
- [44] M. Abdallah *et al.* (STAR Collaboration), Phys. Lett. B **827**, 136941 (2022).
- [45] Y. Nara *et al.*, Phys. Rev. C **61**, 024901 (2000).
- [46] A. S. Botvina, K. K. Gudima, J. Steinheimer, M. Bleicher, and J. Pochodzalla, Phys. Rev. C **95**, 014902 (2017).
- [47] A. S. Botvina, J. Steinheimer, E. Bratkovskaya, M. Bleicher, and J. Pochodzalla, Phys. Lett. B **742**, 7 (2015).
- [48] T. Shao, J. Chen, C. M. Ko, K.-J. Sun, and Z. Xu, Chin. Phys. C **44**, 114001 (2020).
- [49] F. Wang and S. Pratt, Phys. Rev. Lett. **83**, 3138 (1999).
- [50] T. Neidig, K. Gallmeister, C. Greiner, M. Bleicher, and V. Vovchenko, Phys. Lett. B **827**, 136891 (2022).
- [51] T. Reichert, G. Inghirami, and M. Bleicher, Eur. Phys. J. A **56**, 267 (2020).
- [52] J. Cleymans, H. Oeschler, K. Redlich, and S. Wheaton, Phys. Rev. C **73**, 034905 (2006).
- [53] J. Randrup and J. Cleymans, Phys. Rev. C **74**, 047901 (2006).

Supplemental Material: First Observation of Directed Flow of hypernuclei ${}^3_{\Lambda}\text{H}$ and ${}^4_{\Lambda}\text{H}$ in $\sqrt{s_{NN}} = 3$ GeV Au+Au Collisions at RHIC

The STAR Collaboration

I. EVENT PLANE RESOLUTION

In this measurement, the directed flow is calculated via the event-plane method [1]. For each event, the event plane is reconstructed using the Event Plane Detector (EPD) [2]. For the estimation of the resolution for the first-order event plane, please refer to [3] for details. Figure 1 shows the first-order event plane resolution (Top) and the distributions of raw yields for ${}^3_{\Lambda}\text{H}$ 2-body decay and ${}^4_{\Lambda}\text{H}$ as a function of collision centrality (Bottom). Events from centrality 5-40% (shown by the black dashed lines) are selected for analysis to optimize the signal.

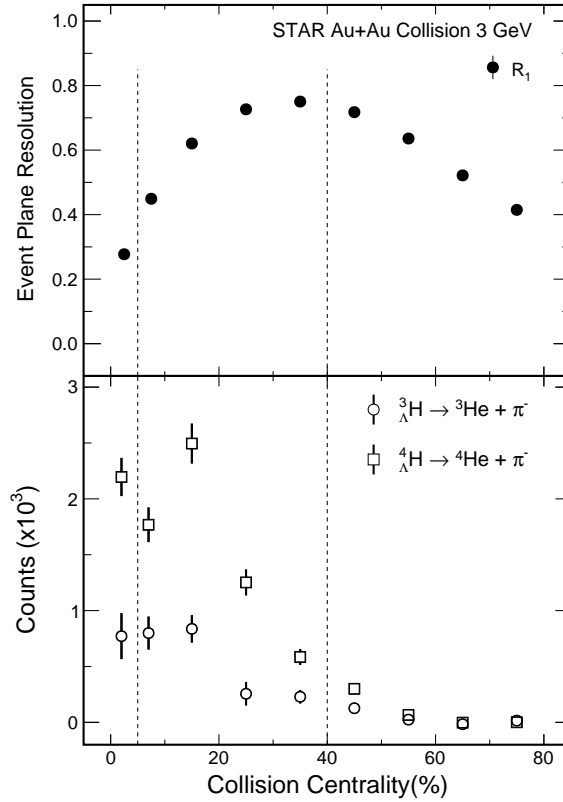


FIG. 1. Top: First-order event plane resolution as a function of collision centrality. Bottom: Distribution of raw yields as a function of collision centrality for ${}^3_{\Lambda}\text{H}$ 2-body decay and ${}^4_{\Lambda}\text{H}$.

II. TOPOLOGICAL CUTS USED FOR Λ , ${}^3_{\Lambda}\text{H}$ AND ${}^4_{\Lambda}\text{H}$

Table I shows topological variables cuts employed for Λ , ${}^3_{\Lambda}\text{H}$, and ${}^4_{\Lambda}\text{H}$ candidate selection. Their definitions are: (1) nHitsFit is the number of TPC points used in the track fitting; (2) l is the decay length from primary vertex to decay vertex; (3) ldl is the distance from the decay point of the candidate to the primary vertex normalized on the error; (4) χ^2_{topo} is the mother particle's χ^2 deviation from the primary vertex; (5) χ^2_{ndf} is the χ^2 deviation between daughter particles; (6) χ^2_{prim} defines the daughter particle's χ^2 deviation from the primary vertex.

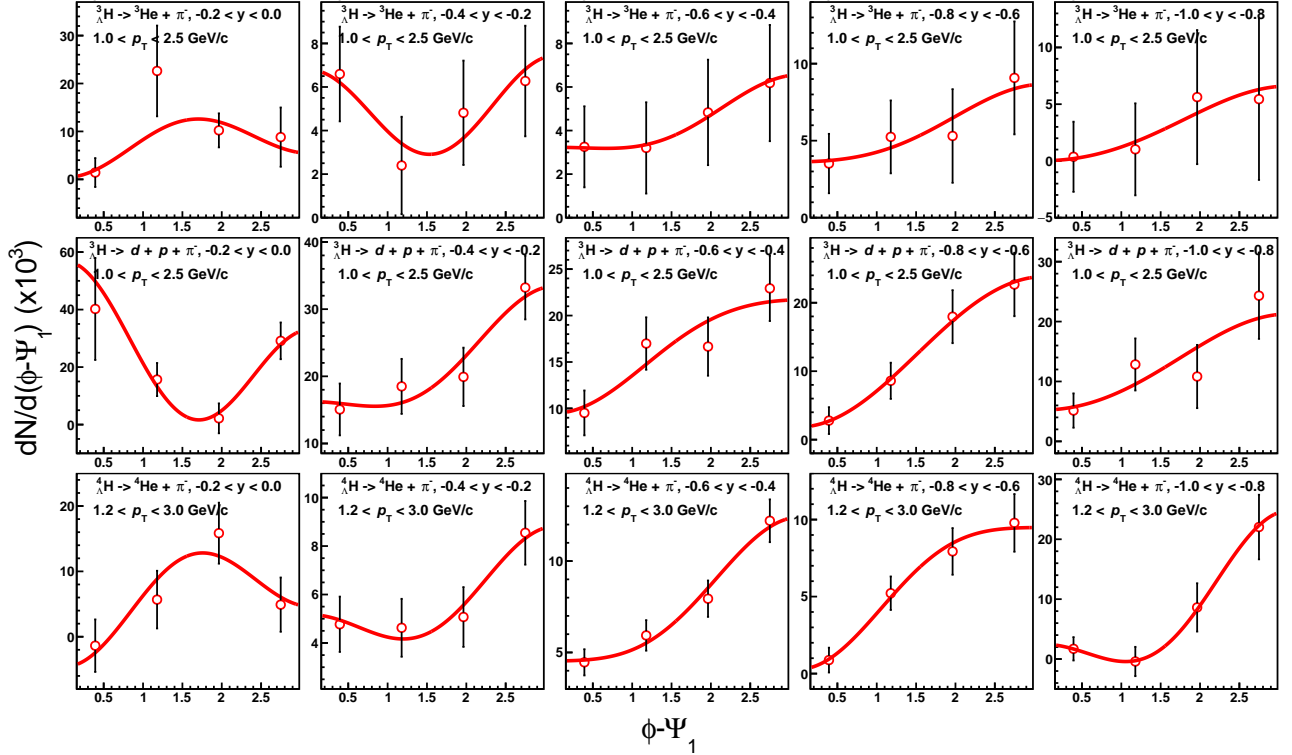
arXiv:2211.16981v2 [nucl-ex] 7 Jun 2023

Particle	Λ	${}^3_\Lambda\text{H}$ (2-body)	${}^3_\Lambda\text{H}$ (3-body)	${}^4_\Lambda\text{H}$
Topological cuts	nHitsFit ≥ 15	nHitsFit ≥ 15	nHitsFit ≥ 15	nHitsFit ≥ 15
	$l > 1$ cm	$l > 2$ cm	$l > 8$ cm	$l > 1.5$ cm
	$ldl > 5$	$ldl > 3$	$ldl > 5$	$ldl > 3$
	$\chi_{topo}^2 < 5$	$\chi_{topo}^2 < 5$	$\chi_{topo}^2 < 3$	$\chi_{topo}^2 < 3$
	$\chi_{ndf}^2 < 5$	$\chi_{ndf}^2 < 5$	$\chi_{ndf}^2 < 3.5$	$\chi_{ndf}^2 < 2$
	$\chi_{prim,p}^2 > 10$	$\chi_{prim,He}^2 > 5$	$\chi_{prim,d}^2 > 0$	$\chi_{prim,He}^2 > 0$
	$\chi_{prim,\pi}^2 > 10$	$\chi_{prim,\pi}^2 > 20$	$\chi_{prim,p}^2 > 5$	$\chi_{prim,\pi}^2 > 10$

TABLE I. Topological cuts used for Λ , ${}^3_\Lambda\text{H}$ and ${}^4_\Lambda\text{H}$.

III. FITTING AZIMUTHAL DISTRIBUTIONS FOR HYPERNUCLEI

Figure 2 shows the distributions of $dN/d(\phi - \Psi_1)$ as a function of $\phi - \Psi_1$ for ${}^3_\Lambda\text{H}$ 2-body and 3-body decay and ${}^4_\Lambda\text{H}$ in different rapidity regions, for centrality bin 5-40%. Distributions of $dN/d(\phi - \Psi_1)$ is fitted by $dN/d(\phi - \Psi_1) = p_0(1 + 2v_1^{obs} \cos(\phi - \Psi_1) + 2v_2^{obs} \cos(2(\phi - \Psi_1)))$, where p_0 , v_1^{obs} and v_2^{obs} are normalization parameter, observed directed and elliptic flows, respectively. In each panel, red lines show the fitting results, which can well describe data points.

FIG. 2. In 3 GeV Au+Au collisions, the angular distributions of ${}^3_\Lambda\text{H}$ 2-body and 3-body decays and ${}^4_\Lambda\text{H}$ in different rapidity regions.

IV. PURITY FOR THE ${}^3_\Lambda\text{H} \rightarrow p + d + \pi^-$ 3-BODY DECAY

The kinematically correlated Λ and deuteron would form a peak around $M(\Lambda) + M(d) = 2.9913$ GeV/ c when $C(k^*) > 1$ at $k^* \rightarrow 0$, where $C(k^*)$ is the kinematic correlation function of Λ and deuteron and k^* is relative momentum between Λ and deuteron. These correlated $\Lambda + d$ pairs would coincide with the reconstructed ${}^3_\Lambda\text{H}$ signals via ${}^3_\Lambda\text{H} \rightarrow p + d + \pi^-$ channel even after combinatorial background subtraction, since ${}^3_\Lambda\text{H}$ is weakly bounded with a small Λ separate energy $B_\Lambda \sim 0.13 - 0.41$ MeV/ c^2 [4] and the finite experimental momentum resolution could not

separate the ${}^3_{\Lambda}\text{H}$ invariant mass peak from the correlated $\Lambda + d$ peak.

Although the invariant masses of correlated $\Lambda + d$ background and the real signal are close, some of their topological kinematics are different. For correlated $\Lambda + d$ background, the decay daughters of $\Lambda \rightarrow p\pi^-$ and deuteron come from different vertices, while the daughters of ${}^3_{\Lambda}\text{H}$ are all produced at the same vertex. χ^2_{NDF} is a topological variable calculated by KFParticle package [5] that characterizes whether particle trajectories intersect at the same vertex within uncertainties. A cut on χ^2_{NDF} can greatly suppress the correlated background. However, these correlated background cannot be fully rejected by such a cut, since Λ daughters and the deuteron could be very close at $k^* \rightarrow 0$ and they cannot be distinguished experimentally due to the finite spatial resolution. Therefore, the template fitting method is used to extract the fraction of ${}^3_{\Lambda}\text{H}$ signal in the reconstructed sample. χ^2_{NDF} distributions of the candidate ${}^3_{\Lambda}\text{H}$ in the data are extracted and then fitted with the template χ^2_{NDF} distributions of correlated background and pure signal. The ${}^3_{\Lambda}\text{H}$ candidates from data are selected within $M({}^3_{\Lambda}\text{H}) \pm 2\sigma$ with all topological cuts used in the analysis applied expect for the χ^2_{NDF} cut. The combinatorial background is estimated by rotating decay daughter particles. The templates for ${}^3_{\Lambda}\text{H}$ signals are obtained from embedding simulated Monte Carlo (MC) ${}^3_{\Lambda}\text{H}$ signal into real data and applying the same reconstruction procedure as in data analysis. Similarly, correlated background templates are built by embedding simulated Λ particles into real data and pairing MC Λ with deuteron tracks from real data. MC Λ are weighted according to the measured Λ spectra. The reconstructed $\Lambda + d$ from embedding are weighted with kinematic correlation functions [6] and applied with the same topological and invariant mass selection cuts as data samples. The χ^2_{NDF} distribution of reconstructed ${}^3_{\Lambda}\text{H}$ candidates are fitted with $f_{\text{data}} = p_0 \cdot (p_1 \cdot f_{\Lambda\text{H}} + f_{\Lambda d})$, where f_{data} , $f_{\Lambda\text{H}}$ and $f_{\Lambda d}$ refer to the normalized χ^2_{NDF} distributions of H3L candidates from real data, H3L and $\Lambda + d$ templates from embedding, respectively. The parameter p_0 and p_1 are fitting parameters. The ${}^3_{\Lambda}\text{H}$ purity, $p_{\Lambda\text{H}}$, is defined as the fraction of ${}^3_{\Lambda}\text{H}$ signal in the reconstructed ${}^3_{\Lambda}\text{H}$ candidates with all topological cuts applied in the data analysis. Figure 3 shows the estimated $p_{\Lambda\text{H}}$ as a function of rapidity. The ${}^3_{\Lambda}\text{H}$ yield is calculated as $p_{\Lambda\text{H}} \cdot N^{\text{raw}}$, where N^{raw} is the raw ${}^3_{\Lambda}\text{H}$ candidate counts.

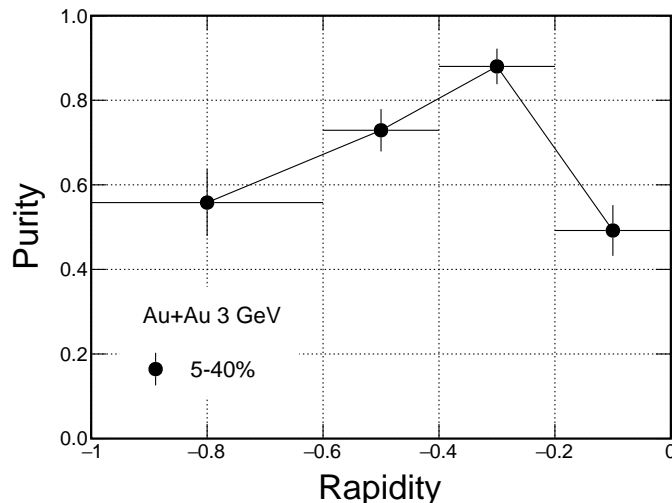


FIG. 3. The estimated purity of ${}^3_{\Lambda}\text{H}$ $p_{\Lambda\text{H}}$ in the reconstructed ${}^3_{\Lambda}\text{H}$ candidate sample via ${}^3_{\Lambda}\text{H} \rightarrow p + d + \pi^-$ as a function of rapidity.

V. MODEL ANALYSIS AND COMPARISON

A. Determine the coalescence parameters from measured hypernuclei $dN/p_T dy dp_T$

Transport models JAM [7, 8] and UrQMD [9] are utilized to generate nucleons and Λ hyperons at 3 GeV. As these models can not reproduce light nuclei and hypernuclei yields, a simple coalescence approach is employed to form light nuclei and hypernuclei using spatial and momentum distributions of nucleons and Λ hyperons at a time of 50 fm/c in the medium evolution. For a hypernucleus, it forms in two steps. Firstly, a light nucleus core is formed based on the relative momentum Δp and relative distance Δr of constituent nucleons in their rest frame. Then the light nucleus core combines with a Λ to form a hypernucleus following a similar process. The coalescence parameters, Δp and Δr ,

are determined by matching the $dN/p_T dy dp_T$ spectrum from the calculations to the corresponding experimental data for a given light nucleus or hypernucleus [10]. The Δp is 0.3 GeV/c for both deuteron and triton, and Δr is 4.5 fm and 4 fm for them, respectively. The Δr is 4 fm for both ${}^3_\Lambda\text{H}$ (deuteron + Λ) and ${}^4_\Lambda\text{H}$ (triton + Λ), and Δp is 0.12 GeV/c and 0.3 GeV/c, respectively. In the model, we assume that the branching ratios are 25% and 50% for ${}^3_\Lambda\text{H} \rightarrow {}^3\text{He} + \pi^-$ and ${}^4_\Lambda\text{H} \rightarrow {}^4\text{He} + \pi^-$, respectively. These results from JAM plus coalescence calculations can qualitatively reproduce the ${}^3_\Lambda\text{H}$ and ${}^4_\Lambda\text{H}$ spectra [10], as show in Fig. 4.

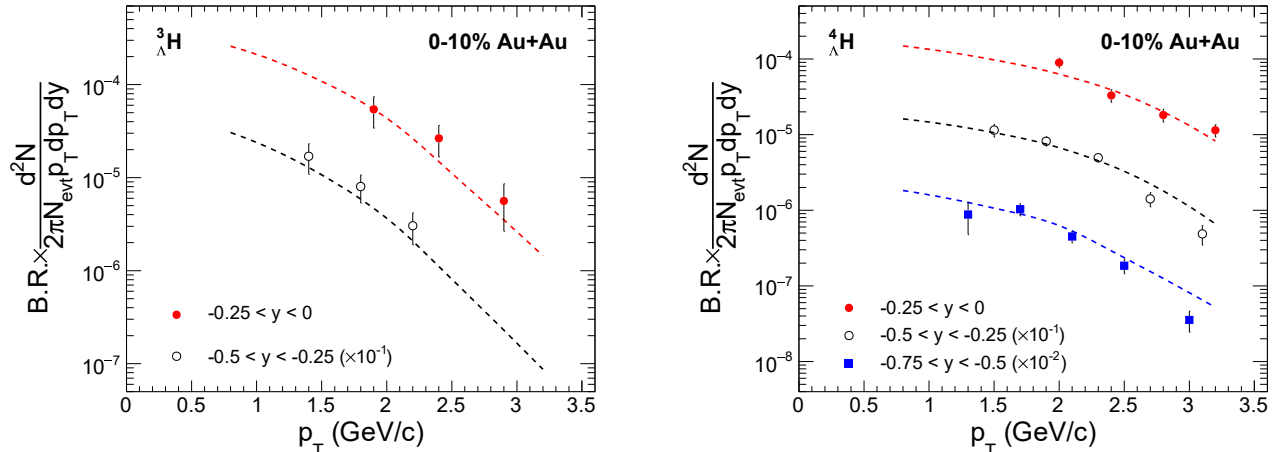


FIG. 4. ${}^3_\Lambda\text{H}$ and ${}^4_\Lambda\text{H}$ p_T spectra in three different rapidity intervals from 0-10% central Au+Au collisions at $\sqrt{s_{NN}} = 3$ GeV. Only the statistical uncertainties are plotted. The dashed lines are results from JAM plus coalescence calculations. For model results, spectra are scaled with the branching ratios which are assumed to be 25% and 50% for ${}^3_\Lambda\text{H} \rightarrow {}^3\text{He} + \pi^-$ and ${}^4_\Lambda\text{H} \rightarrow {}^4\text{He} + \pi^-$, respectively [10].

B. $v_1(y)$ distributions from JAM and UrQMD model calculations

Figure 5 shows the Λ hyperon and hypernuclei directed flow v_1 , as a function of rapidity, from the $\sqrt{s_{NN}} = 3$ GeV 5-40% mid-central Au + Au collisions. The results of a linear fit:

$$v_1(y) = v_1^s \cdot y \quad (1)$$

for ${}^3_\Lambda\text{H}$ and ${}^4_\Lambda\text{H}$ are shown as red-yellow lines in the figure. The range of $(-1.0 < y < 0)$ is used for v_1 measurements of all light nuclei, Λ hyperon and hypernuclei, as well as their model results. As the Λ and light nuclei have an obvious non-linear tendency at $y < -0.5$. So a 1st plus 3rd order polynomial function

$$v_1(y) = v_1^s \cdot y + p_1 \cdot y^3 \quad (2)$$

is used to fit them. The same fitting procedure is applied to model calculations, as well as to the ${}^3_\Lambda\text{H}$ and ${}^4_\Lambda\text{H}$ model calculations. While for the v_1 results from ${}^3_\Lambda\text{H}$ and ${}^4_\Lambda\text{H}$, due to the limitation of their statistics, we use the 1st order polynomial function to describe them. In Fig. 5, transport model calculations (fit results) from JAM and UrQMD are shown as cross circles and cross squares (long dashed and dot-dashed lines), respectively. The resulting mid-rapidity v_1 slopes for all the particles under study are summarized in Fig. 4 of the manuscript.

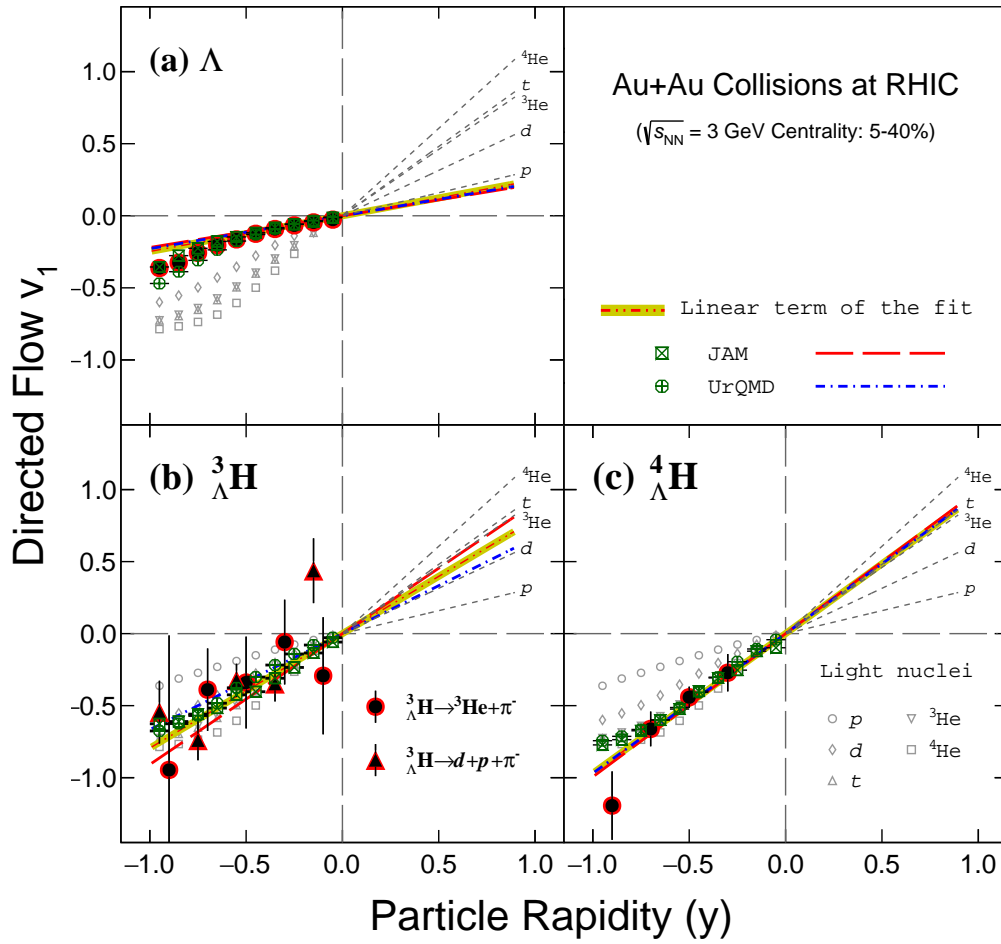


FIG. 5. Λ hyperon and hypernuclei directed flow v_1 , shown as a function of rapidity, from the $\sqrt{s_{NN}} = 3$ GeV 5-40% mid-central Au + Au collisions. In case of ${}^3_{\Lambda}\text{H}$ v_1 , both results from 2-body (circles) and 3-body (triangles) decays are shown. The fitted linear terms for light nuclei are plotted as dashed lines in the positive rapidity region, while for Λ hyperon, ${}^3_{\Lambda}\text{H}$ and ${}^4_{\Lambda}\text{H}$, they are shown by the yellow-red lines in the corresponding panels. The rapidity dependence of v_1 for p , d , t , ${}^3\text{He}$, and ${}^4\text{He}$ are also shown as open markers, including circles, diamonds, up-triangles, down-triangles and squares, respectively. The corresponding v_1 results extracted from 1st+3rd order polynomial fits, within $-1.0 < y < 0$, are shown as dashed lines in the positive rapidity region. Transport model calculations (fit results) from JAM and UrQMD are shown as cross circles and cross squares (long dashed and dot-dashed lines), respectively.

-
- [1] Hiroshi Masui, Alexander Schmah, and A.M. Poskanzer. Event plane resolution correction for azimuthal anisotropy in wide centrality bins. *Nuclear Instruments and Methods in Physics Research Section A: Accelerators, Spectrometers, Detectors and Associated Equipment*, 833:181–185, Oct 2016.
 - [2] Joseph Adams et al. The STAR Event Plane Detector. *Nucl. Instrum. Meth. A*, 968:163970, 2020.
 - [3] M. S. Abdallah et al. Disappearance of partonic collectivity in sNN=3GeV Au+Au collisions at RHIC. *Phys. Lett. B*, 827:137003, 2022.
 - [4] Jaroslav Adam et al. Measurement of the mass difference and the binding energy of the hypertriton and antihypertriton. *Nature Phys.*, 16(4):409–412, 2020.
 - [5] Maksym Zyzak. *Online selection of short-lived particles on many-core computer architectures in the CBM experiment at FAIR*. PhD thesis, Frankfurt U., 2016.
 - [6] J. Haidenbauer. Exploring the Λ -deuteron interaction via correlations in heavy-ion collisions. *Phys. Rev. C*, 102(3):034001, 2020.
 - [7] Y. Nara et al. Study of relativistic nuclear collisions at AGS energies from p + Be to Au + Au with hadronic cascade model. *Phys. Rev. C*, 61:024901, 2000.
 - [8] Yasushi Nara, Harri Niemi, Akira Ohnishi, and Horst Stöcker. Examination of directed flow as a signature of the softest point of the equation of state in QCD matter. *Phys. Rev. C*, 94(3):034906, 2016.
 - [9] J. Steinheimer, J. Auvinen, H. Petersen, M. Bleicher, and H. Stöcker. Examination of directed flow as a signal for a phase transition in relativistic nuclear collisions. *Phys. Rev. C*, 89(5):054913, 2014.
 - [10] Mohamed Abdallah et al. Measurements of $\text{H}\Lambda 3$ and $\text{H}\Lambda 4$ Lifetimes and Yields in Au+Au Collisions in the High Baryon Density Region. *Phys. Rev. Lett.*, 128(20):202301, 2022.